

# **A phase-field model for simulating pitting corrosion**

A project  
Submitted for the fulfillment of Degree of

**Master of Engineering**

in Materials Engineering

By

**Pramod Kumar**

Supervisor

**Dr. Abhik Choudhury**



Department of Materials Engineering  
Indian Institute of Science  
Bangalore - 560012 , India  
June 2016

---

Dedicated to  
My teachers

---

# *Acknowledgements*

Although language has limitations to convey the feelings along with words, I'll try my best to express my sincere gratitude to my advisers, colleagues, seniors and family, for their help and support throughout my masters project, without which it would have been difficult to make it a reality.

First and foremost, I would like to thank my adviser Dr. Abhik Chaudhury for his guidance, continuous support and never ending patience during my ME project and thesis writing. Working with Dr. Abhik is an unforgettable experience which has really boosted my knowledge in ME project, material science and refined my approach and attitude toward solving the problems. I am really thankful to him for giving me a lot of opportunities to share my views and offering constructive criticism which have been instrumental to conclude the project.

I would like to thank Prof. T.A. Abinandanan, my research adviser and chairman of the Department of Materials Engineering, IISc, Bangalore, for allowing me to use departmental computational facilities and giving me valuable advise whenever needed.

I am also indebted to my lab mates(Prof. Abinandanan's lab ), Kamalnath, Bhaskar, Chaitanya and Naveen, for their help, no matter how trivial my questions were they were solved with infinite patience.

I would like to express my gratitude to my lab mates (Dr. Abhik's lab) Arka lahiri, Bunt, Supriyo, and Apaar for their continuous support and help at every stage of project.

I am always grateful to my batch mates who are some of the best people I know, Chaitali, Urvashi, Prachi, Indrani, Anwisha, Awadh, Subhash, Sai, Rakesh, Antareep, Kaustubh, Abhishek, Supriyo and Rahul. It is impossible to forget all the logical discussions on illogical topics with Subhash, Awadh, Rakesh, Indrani and Prachi, over drinks (Tea and Coffee in prakriti). My sincerest regards to Rani rohini (Rani didi) for always treating me as a younger brother. Special thanks to Sharan and Arka.

Finally, I would like to mention the overwhelming support from my sisters Anjali, Arti, and Jyoti, who always kept me motivated during all the ups and downs of my life. I would like to mention the love and support of my parents, which still keeps me motivated even today. They will always be missed from the deepest of my heart.

It is impossible to write everything in words but I am thankful to everybody in the department, friend circle and family for always being there when I needed.

# Contents

List of Figures	ii
1 Introduction and Motivation	1
2 Phase-field model	4
2.1 Generic phase-field model . . . . .	5
2.1.1 The electrostatic potential . . . . .	7
2.1.2 Reaction rates . . . . .	8
2.2 Modeling single-phase dissolution . . . . .	8
2.2.1 Determining the coefficients . . . . .	10
3 Kinetics of the pitting reaction: Geometry effects	11
3.1 Boundary and initial Conditions . . . . .	11
3.2 Simulation studies . . . . .	12
3.3 Auto-catalytic nature . . . . .	15
4 Pitting in three-phase regions	17
4.1 Grooving . . . . .	18
4.2 Grooving coupled with pitting . . . . .	18
4.3 Inter-Granular corrosion . . . . .	21
4.3.1 Model modifications . . . . .	22
4.3.2 Simulation studies . . . . .	22
5 Conclusions	27
Bibliography	28

# List of Figures

3.1	The red regions in (a) represent the substrate and the blue regions the electrolyte. From (a) to (d) the Cl <sup>-</sup> concentration develops from an uniform composition in the electrolyte indicated by the blue color to a inhomogeneous distribution as the pitting reaction proceeds. This is evident with the higher concentration of Cl <sup>-</sup> at the pit. . . . .	13
3.2	Plot showing the binary interface contour and its development over time. A comparison between initial and final condition for two different widths of the initial pit, in (a) width=20 and in (b) width = 28. . . . .	13
3.3	Plot showing the binary interface contour and its development over time. A comparison between initial and final condition for two different widths and depths of the initial pit, in (a) width=20, depth=12, (b) width=20, depth=14, (c) width=28, depth=12, (d) width=28, depth=14 . . . . .	14
3.4	Interface profiles at various times, keeping the time interval constant between two consecutive interface profiles, in (a)width 28, depth 10 and (b) width 28, depth 12 . . . . .	16
4.1	Plots showing the interface position at different times during the grooving process for different values of $\gamma_{sl}$ , in (a) $\gamma_{sl} = 1.0$ , (b) $\gamma_{sl} = 0.8$ , (c) $\gamma_{sl} = 0.6$ and (d) shows the compares all the interface positions at a given time. . . . .	18
4.2	Plot showing the binary interface contour and comparison between the cases of electrochemical attack in combination with grooving, with just the grooving process, for three different triple point geometries created by the choice of three different values of the surface energies $\gamma_{sl}$ , which is for (a) $\gamma_{sl} = 1.0$ , (b) $\gamma_{sl} = 0.8$ and (c) $\gamma_{sl} = 0.6$ . The plots are normalized to bring out the differences between the evolution process brought about due to electrochemical corrosion. . . . .	19

4.3 Plot showing the binary interface contour for different rate constants at separate times during evolution. In (a)  $t=500000$ , (b)  $t=1000000$ , (c)  $t=3000000$ . . . . . 21

4.4 Interface contours plotting the progress of the inter-granular corrosion process for three different reaction rate constants for the dissolution process, in (a) rate constant = 0.00001, (b) rate constant = 0.00002 and (c) rate constant = 0.00003. . . . . 24

4.5 Interface plots showing comparison between the cases of pure grooving and under the influence of inter-granular attack for two different reaction rates, in (a) rate constant=0.00001, and (b) rate constant=0.00003. . . 24

4.6 Comparison of IGC for rate constant= .00001 for various surface energy values . . . . . 25

4.7 Interface profiles showing the pit formation at different times for three different conditions of just grooving and two different values of critical concentration of Cr below which the pitting reaction is activated. In (a) and (b) which are plots corresponding to time  $t=1000000$  and  $t=2000000$  respectively, there is no difference in the evolution between the plots showing jut grooving dynamics and electrochemical attack, while in (c) which is for  $t=3000000$ , there is increased pit formation for the case of lower Cr content. . . . . 26

# Introduction and Motivation

Corrosion is a process of degradation of material, by chemical or electrochemical reactions with its environment. Corrosion can be localized or uniform in nature. If the entire material is exposed to electrolyte and there is no specific location for electrolyte to attack, this condition leads to the uniform corrosion. Uniform corrosion although detrimental, is not the most harmful types of corrosion. It is the *localization* of the corrosion process which is the more prevalent reason for the reduction of component life, as one of the foremost consequences of concentrated corrosive attack leads to regions of high stress intensity and therefore materials become prone to damage by mechanical failure leading to considerably shortening in the service life of the material. Such, localized corrosion will take place if there is any chemical/mechanical damage of protective layer of the alloy, at very high density region of dislocation, at the precipitate/matrix boundaries which is anodic or cathodic to the matrix, inclusion which applies stress field to the matrix etc. Pitting corrosion is one of the forms of corrosion, generally leading to localized damage of the material, which will be the focus of our modeling exercise in this thesis work.

The pitting process involves the dissolution of metal ions at locations on the surface where there are deep depressions also called *pits*. The dissolution reaction occurring at such locations are typically auto-catalytic, i.e the reaction rate increases with increase in the depth of pit. The process of dissolution involves a coupling of the anodic reaction which leads to the loss of the metal and a cathodic reaction, which involves the combination of dissolved oxygen with hydrogen ions and electrons. On a flat surface, the rates of both of these reactions occurs equally fast, resulting in the occurrence of uniform corrosion. However, in the presence of a pit, the reaction products which are for example  $Al^{3+}$  ions in an aluminium alloy get accumulated in the pit leading to larger concentrations at the interface. This draws in  $Cl^-$  ions from the surrounding environment as a consequence of electrostatic potential gradients, which tends to fasten the dissolution reaction. The mechanism behind this, is still an open question and one

of the proposed pathways is that the  $Cl^-$  is involved in a reaction which forms a salt with the  $Al^{3+}$  ions in the pit, thereby the concentration of the  $Al^{3+}$  ions is depleted which increases the overpotential of the dissolution reaction and thus maintains a high dissolution rate. Barring this reaction, the  $Al^{3+}$  at the interface reduces in value just by diffusion into the electrolyte, which occurs on much larger time-scales. The difference in the dissolution rates at the surface and the pit is therefore a function of the difference in  $Cl^-$  concentrations at the two locations, thereby causing deepening of the pit, which increases the concentration differential of the  $Cl^-$  concentration differences between the surface and the pit, consequently, fastening the rate of pit growth. This is why it is also called an auto-catalytic process.

The other proposed possibility is that the  $Cl^-$  concentration alters the stability of the passive layer that usually forms, thereby regions with higher concentrations of  $Cl^-$  ions have a more active interface with respect to the dissolution process. This mechanism also reflects the auto-catalytic nature of the pit growth process.

Phase-field modeling has been used extensively for the investigation of interfacial pattern formation in many areas [2, 7, 12], and therefore it seems natural to use this strategy here. While, there are other model descriptions for the pitting corrosion process which are described in [1] and [13] both of which are based on the cellular-automaton technique, we will adopt certain ideas from these formulations into a phase-field formulation which is more amenable to interface driven problems.

In the literature, there are a number of models written down for the application to problems involving electrochemical reactions. However, none of those are immediately applicable here. Guyer *et al.* [5, 6] discuss a general description for electrochemical reactions in phase-field models, but the resulting model is limited to the nanometer scale due to the required fine discretization. Other models include electromigration terms, but assume charge neutrality everywhere [9–11], which excludes the description of the space-charge region.

In this thesis, there are three major focus areas of our work,

- Proposing a novel phase-field model capturing the auto-catalytic mechanism of the pitting process in a generic metal electrolyte system.
- Utilizing the model for understanding the factors relating to the pit geometry, which aid in either fastening the pit growth or impeding it.
- Extending the model for capturing the pit growth in a grain-boundary, and again



characterizing the reaction based on the shape of the grain-boundary pits through the variation of the grain-boundary energies.

- Modeling a concentrated form of attack, such as inter-granular corrosion, where a reaction involving a protective element at the grain-boundary leads to depletion of this element, thereby exposing the material to concentrated attack. Here as well, we will study the corrosion process as a function of the various pit geometry which is altered by changing the relative grain-boundary energies.

The rest of the thesis work is divided into the following parts, Chapter 2 discusses the phase-field model. Chapter 3 elaborates on the characteristics of the pitting reaction as a function of the pitting geometry. Chapter 4, highlights the characteristics of the pitting reaction at a grain boundary and Chapter 5 extends the study of reactions at grain boundaries where there is concentrated attack due to depletion of the protective element as a result of a separate reaction. Chapter 6 concludes the thesis work with a summary of the main results. Also all our results with respect to distances will be in terms of non-dimensional units.

# Phase-field model

In this thesis, we propose a model which captures the basic auto-catalytic nature of pit growth, using the electrochemical cathodic and anodic reactions with occurring at the interface. Electrochemical reactions are the reactions in which charge is transferred from an atom to another atom, through an electron conducting medium, electrode. Electrochemical reaction always need two conductors one is an electron conductor and the other an ionic conductor. The electron donating reaction is called the *anodic* half cell reaction and the electron accepting reaction is called *cathodic* half cell reaction, which is collectively called electrochemical cell. In the pitting reaction constant the anodic reaction results in the dissolution of the metal, while the electrons used up in the formation of water molecules in the cathodic half cell.

In this particular phase-field formulation, we will utilize the order-parameter vector  $\boldsymbol{\phi} = \{\phi_\alpha \dots \phi_N\}$  where each of the constituents  $\phi_\alpha$  to  $\phi_N$  represents the volume fractions of the phases 1 to N in the system. In essence this set of order parameters are functions of space and will be used in the spirit of indicator functions, which demarcate the regions of space where a particular phase exist. Therefore, the phase-field variables  $\phi_i$  constituting the vector are bounded functions whose values range from 0 to 1 while, on account of being used of volume fractions, they obey an additional constraint  $\sum_{i=\alpha}^N \phi_i = 1$  at every point in the domain. The diffusion potential vector  $\boldsymbol{\mu} = \{\mu_1 \dots \mu_K\}$  is going to be the other state variable determining the spatial variation of the diffusion potentials of the different species. Finally, some of the components are going to be charged in the electrochemical system, there are electrostatic potential differences that will be required to be solved for. Thus, the electrostatic potential  $V$  will be the third state-variable defining the evolution of the system.

## 2.1 Generic phase-field model

In this section, we give a brief description of the employed phase-field model as also published in [3]. Phase evolution is determined by the phenomenological minimization of the *grand canonical density functional* written as,

$$\Omega(\boldsymbol{\mu}, \boldsymbol{\phi}) = \int_{\Omega} \left( \Psi(\boldsymbol{\mu}, \boldsymbol{\phi}) + \left( \epsilon a(\boldsymbol{\phi}, \nabla \boldsymbol{\phi}) + \frac{1}{\epsilon} w(\boldsymbol{\phi}) \right) \right) d\Omega, \quad (2.1)$$

where  $\epsilon$  is the length scale related to the interface, and  $\boldsymbol{\phi}$  is the phase-field vector containing the volume fractions of the  $N$ -phases. We write the grand potential density  $\Psi$ , as an interpolation of the individual grand potential densities  $\Psi^\alpha$ , where  $\Psi^\alpha$  are functions of the diffusion potential  $\boldsymbol{\mu}$ ,

$$\Psi(\boldsymbol{\mu}, \boldsymbol{\phi}) = \sum_{\alpha=1}^N \Psi^\alpha(\boldsymbol{\mu}) h_\alpha(\boldsymbol{\phi}) \quad . \quad (2.2)$$

In the grand-potential density, we incorporate the thermodynamic functions, which are going to be described below.  $h_\alpha(\boldsymbol{\phi})$  is the interpolation polynomial written as  $h_\alpha(\boldsymbol{\phi}) = \phi_\alpha^2 (3 - 2\phi_\alpha) + 2\phi_\alpha \sum_{\beta \neq \alpha, \gamma \neq \alpha}^{N,N} \phi_\beta \phi_\gamma$ , which ensures that  $\sum_{\nu}^N h_\nu(\boldsymbol{\phi}) = 1$ . The phase concentration expressions can be derived in terms of the diffusion potential using the relation  $c_i^\alpha(\tilde{\boldsymbol{\mu}}^m) = -V_m \frac{\partial \Psi^\alpha(\boldsymbol{\mu})}{\partial \mu_i}$ . Thereafter, the equations of motion for the phase-field and the composition variables are derived in a standard manner.

The evolution equations for the  $N$  phase-field variables  $\phi_\alpha, \alpha = \{1, \dots, N\}$  can be derived as,

$$\tau \epsilon \frac{\partial \phi_\alpha}{\partial t} = \epsilon \left( \nabla \cdot \frac{\partial a(\boldsymbol{\phi}, \nabla \boldsymbol{\phi})}{\partial \nabla \phi_\alpha} - \frac{\partial a(\boldsymbol{\phi}, \nabla \boldsymbol{\phi})}{\partial \phi_\alpha} \right) - \frac{1}{\epsilon} \frac{\partial w(\boldsymbol{\phi})}{\partial \phi_\alpha} - \frac{\partial \Psi(\tilde{\boldsymbol{\mu}}^m, \boldsymbol{\phi})}{\partial \phi_\alpha} - \Lambda, \quad (2.3)$$

where  $\Lambda$  is the Lagrange parameter to maintain the constraint  $\sum_{\alpha=1}^N \phi_\alpha = 1$  and the parameter  $\tau$  is written as  $\frac{\sum_{\alpha < \beta}^{N,N} \tau_{\alpha\beta} \phi_\alpha \phi_\beta}{\sum_{\alpha < \beta}^{N,N} \phi_\alpha \phi_\beta}$ , where  $\tau_{\alpha\beta}$  is the relaxation constant of the  $\alpha$ - $\beta$  interface.  $a(\boldsymbol{\phi}, \nabla \boldsymbol{\phi})$  represents the gradient energy density and  $w$  is the surface potential density as a double obstacle function. The function  $a(\boldsymbol{\phi}, \nabla \boldsymbol{\phi})$  and  $w(\boldsymbol{\phi})$  read,

$$a(\phi, \nabla \phi) = \sum_{\alpha < \beta} \gamma_{\alpha\beta} |q_{\alpha\beta}|^2 \quad (2.4)$$

$$w(\phi) = \frac{16}{\pi^2} \sum_{\alpha < \beta} \gamma_{\alpha\beta} \phi_\alpha \phi_\beta + \sum_{\alpha < \beta < \delta} \gamma_{\alpha\beta\delta} \phi_\alpha \phi_\beta \phi_\delta \quad \forall \quad \phi_\alpha \in [0, 1] \quad \text{else} \quad \infty. \quad (2.5)$$

The terms  $\gamma_{\alpha\beta}$  represent numerically the interfacial energies of the  $\alpha\beta$  interface, while  $\gamma_{\alpha\beta\delta}$  is a third-order penalty term utilized for avoiding third and higher order phase adsorption at binary interfaces. The function  $q_{\alpha\beta}$  is the gradient term which reads  $|\phi_\alpha \nabla \phi_\beta - \phi_\beta \nabla \phi_\alpha|$ , [4, 8].

For a general multi-phase, multi-component system, the evolution equations for the components of the diffusion potential  $\boldsymbol{\mu}$  can be expressed in vector-matrix form by,

$$\left\{ \frac{\partial \mu_i}{\partial t} \right\} = \left[ \sum_{\alpha=1}^N h_\alpha(\phi) \frac{\partial c_i^\alpha(\boldsymbol{\mu})}{\partial \mu_j} \right]_{ij}^{-1} \left\{ \nabla \cdot \sum_{j=1}^K M_{ij}(\phi) \nabla (\mu_j + q_j V) - \sum_{\alpha}^N c_i^\alpha(\boldsymbol{\mu}) \frac{\partial h_\alpha(\phi)}{\partial t} + R_i \right\}. \quad (2.6)$$

where  $\{\}$  represents a vector of dimension ( $K$ ) while  $[\cdot]$  denotes a matrix of dimension of dimension ( $K \times K$ ).  $V$  is the electrostatic potential which will be derived such that charge neutrality is maintained at every time-step, while  $q_j$  is the charge per mole of the particular ionic species. The procedure and equations for this calculation of the electrostatic potential will be derived below.  $R_i$  is the rate of production of the ions due to a chemical reaction, which also will be described in the following sections.

Here,  $M_{ij}(\phi)$  is the mobility of the interface, where the individual phase mobilities are interpolated as,

$$M_{ij}(\phi) = \sum_{\alpha=1}^N M_{ij}^\alpha g_\alpha(\phi),$$

where the function  $g_\alpha(\phi) = \phi_\alpha$  interpolates the mobilities. Each of the  $M_{ij}^\alpha$  is defined using the expression,

$$M_{ij}^\alpha = \sum_{k=1}^K D_{ik}^\alpha \frac{\partial c_k^\alpha(\boldsymbol{\mu})}{\partial \mu_j}.$$

$D_{ij}^\alpha$  are the inter-diffusivities in each phase  $\alpha$  and  $\frac{\partial c_k^\alpha(\boldsymbol{\mu})}{\partial \mu_j}$  is the susceptibility  $\chi_{ij}^\alpha$ .

### 2.1.1 The electrostatic potential

In this formulation, we assume that the entire system is at all the time remaining charge neutral. The basis for this assumption is the fact that given that the mobility of the ions in both the electrolyte and the substrates are relatively high, giving rise to low relaxation times for achieving charge neutrality. Also, the phenomenon of pitting that we are considering is independent on the nature of the electrolytic interface and thereby assuming a charge neutral system, also implies that there is no-charge separation at the interface like in the double-layer of an electrolytic interface. This allows us to upscale the length scale to actually capture the mechanism of pitting with better computational flexibility.

It is noteworthy to state an important fact. The assumption of charge neutrality does not imply that the Poisson equation which follows from Gauss-law, can be solved with zero charge density to derive the electrostatic potential profiles. Rather, the condition of charge neutrality requires that local currents due to the electrostatic potentials are such that the eventual diffusion currents result in a charge neutral condition.

The electrostatic potential is therefore derived by writing the expression for the total charge generated per unit time at a grid-point is going to be zero. This gives a set of equations, are Poisson equations need to be simultaneously solved for all the grid-points in the domain to derive the solution for the electrostatic field at every given time-step. The set of equations to be solved for thus derives from the mass-conservation equation, Eqn.2.6 as,

$$\sum_{i=1}^K q_i \left\{ \nabla \cdot \sum_{j=1}^K M_{ij}(\phi) \nabla (\mu_j + q_j V) - \sum_{\alpha}^N c_i^\alpha(\boldsymbol{\mu}) \frac{\partial h_\alpha(\phi)}{\partial t} + R_i \right\} = 0, \quad (2.7)$$

which can be converted into a Poisson-equation as,

$$\sum_{i=1}^K q_i \nabla \cdot \sum_{j=1}^K M_{ij}(\phi) \nabla q_j V = - \sum_{i=1}^K q_i \left\{ \nabla \cdot \sum_{j=1}^K M_{ij}(\phi) \nabla \mu_j - \sum_{\alpha}^N c_i^\alpha(\boldsymbol{\mu}) \frac{\partial h_\alpha(\phi)}{\partial t} + R_i \right\} \quad (2.8)$$

### 2.1.2 Reaction rates

Electrochemical reaction rates giving rise to the production and destruction of ions is derived from Butler-Volmer electrode kinetics. The Butler-Volmer type kinetics which is linearized for the simplicity which writes as,

$$r_i = j_o \left( \sum_i^R \mu_i - \sum_j^P \mu_j \right) \phi_\alpha \phi_\beta \quad (2.9)$$

where the subscripts  $R$  and  $P$  represent reactants and products, and  $j_o$  is the exchange current density. The total reaction rate  $R_i$  is determined by multiplying  $r_i$  with the stoichiometric coefficient for that particular component in the reaction and summing over all the reactions in which the elements takes part. Also, the pre-factor limits it the reaction to the substrate-electrolyte interface.

For the anodic reaction (dissolution of the metal) we make an additional assumption that the rate of dissolution is very fast and that the reaction rate constant is relatively constant and independent of the local overpotential. The cathodic reaction proceeds given the local overpotential (difference of the chemical potentials of the products and the reactants) at a given location. The crux of capturing the auto-catalytic nature of the process is to relate the rate of the dissolution reaction with the local  $Cl^-$  concentration. In the present formulation we utilize an approximate ansatz, where the rate constant controlling the anodic dissolution is proportional to the local  $Cl^-$  composition. Following, is the elaboration on the different parts of the model:

## 2.2 Modeling single-phase dissolution

For the particular case of a single material getting dissolved due to a electrochemical reaction the phase vector writes  $\phi = \{\phi_\alpha, \phi_\beta\}$  where  $\phi_1$  represents the volume fraction of the substrate and  $\phi_2$  the electrolyte. The thermodynamics of the system involves the following components,  $\{Al, Al^{3+}, O_2, H^+, H_2O, Cl^-, e^-, Na^+\}$ . The dissolution of the substrate occurs through the loss of Al atoms to the electrolyte solution, through the formation of  $Al^{3+}$  ions. The chemical thermodynamics of these will be described as follows, since the substrate is high in concentration of Al we follow a parabolic free-energy formulation for the Al ions, while for the other elements given their low chemical

composition, we use a dilute solution approximation.

Therefore the chemical free energy of the each of the phases writes as,

$$f^{\alpha,\beta} = A^{\alpha,\beta} c_{Al}^2 + B_{Al}^{\alpha,\beta} c_{Al} + C^{\alpha,\beta} + \sum_{k \neq Al} B_K^{\alpha,\beta} c_K + (c_K \log c_K - c_K). \quad (2.10)$$

For deriving the driving force for phase transformation, we make an approximation, that change in *Al* concentration principally determines the driving force for the dissolution reaction. This is reasonable, since the magnitude of the other compositions is very small and thereby their leading order contribution to the thermodynamic driving force is going to be small. Thus, the relevant free, energies of the phases for deriving the driving force is written as,

$$\tilde{f}^{\alpha,\beta} = A^{\alpha,\beta} c_{Al}^2 + B_{Al}^{\alpha,\beta} c_{Al} + C^{\alpha,\beta}. \quad (2.11)$$

The driving force itself for the  $\alpha$  to  $\beta$  transition which determines dissolution, is determined by the difference of the grand-potentials,  $\Psi^\alpha - \Psi^\beta$ , which are determined by the Legendre transforms of the free-energy densities  $\tilde{f}$ . This requires one to first transform, the compositions into functions of the diffusion potential, which is readily done, using the derivatives of the free-energy densities of the phases as,  $\mu_{Al} = A_{Al} c_{Al} + B_{Al}$  or  $c_{Al}^{\alpha,\beta}(\mu_{Al}) = \frac{\mu_{Al} - B_{Al}^{\alpha,\beta}}{A_{Al}^{\alpha,\beta}}$ . Using these phase composition relations, Legendre transform of the free.energy densities( $f^\alpha - \mu c$ ) yielding the grand-potential densities derive as,

$$\Psi^{\alpha,\beta} = -A^{\alpha,\beta} \left( \frac{\mu_{Al} - B_{Al}^{\alpha,\beta}}{A_{Al}^{\alpha,\beta}} \right)^2 + C^{\alpha,\beta}. \quad (2.12)$$

For the other components, the free-energy densities of the phases are utilized for determining the diffusion potentials, which are then used for determining the driving force for diffusion.

### 2.2.1 Determining the coefficients

We start with the aim of constructing a system with the given equilibrium compositions for the elements in the substrate and the electrolyte. The coefficients  $A^\alpha$  and  $A^\beta$  are set to 1.0. The coefficients  $B_{Al}^\beta$  and  $C^\beta$  is set to zero. The corresponding values for the  $\alpha$  phase is determined by setting the condition that  $\mu_{Al}$  is the same in both phases and  $\Psi^\beta - \Psi^\alpha = 0$ .

For the coefficients of the dilute elements,  $B_k^{\alpha,\beta}$  are determined through the following procedure. For all the components except  $Al3+$  and  $H20$  the coefficients  $B_k^\beta$  is set to zero. For these two components, the coefficient  $B$  is determined by the condition that the reaction rates of the anodic and cathodic reactions determined by the linearized Butler-Volmer equations is set to zero. Thereafter, the other coefficients in the both the phases are determined by the condition, that the diffusion potential  $\mu_i$  in both the phases are equal. Please note, ensuring the condition of equality of diffusion potential along with the condition of reaction equilibrium for both the cathodic and anodic reaction in the electrolyte phase, ensures that the reaction is at equilibrium also in the substrate phase.



# Kinetics of the pitting reaction: Geometry effects

The model has been first applied for the pitting corrosion. which consists of different pit geometries, in order to ascertain the pit growth rates as a function of pit geometry. In particular, we initialize the system, with a pit of defined width and depth and study its evolution as a function of time, for a fixed set of growth conditions. The substrate phase is named  $\alpha$  and the electrolyte as  $\beta$ . The equilibrium phase compositions of the substrate are assumed as,  $c_{Al} = 1.0, c_{Al3+} = 0.0001, c_{O2} = 0.00001, c_{H+} = 0.0001, c_{H2O} = 0.0001, c_{Cl-} = 0.0003, c_{e-} = 0.01, c_{Na+} = 0.0001$ , while the electrolyte the compositions, are assumed to be  $c_{Al} = 0.0, c_{Al3+} = 0.0001, c_{O2} = 0.1, c_{H+} = 0.1, c_{H2O} = 0.1, c_{Cl-} = 0.1002, c_{e-} = 0.0001, c_{Na+} = 0.05$ . For the inter-diffusivity matrix only diagonal diffusivity of the different species is assumed. Following are the inter-diffusivity values for the different species in the substrate:  $D_{Al} = 0.01, D_{Al3+} = 0.3, D_{O2} = 0.01, D_{H+} = 0.01, D_{H2O} = 0.01, D_{Cl-} = 0.01, D_{e-} = 10.0, D_{Na+} = 0.01$ , while for the electrolyte the diffusivities of the different species is given by,  $D_{Al} = 0.01, D_{Al3+} = 0.1, D_{O2} = 5.0, D_{H+} = 10.0, D_{H2O} = 0.1, D_{Cl-} = 10.0, D_{e-} = 0.01, D_{Na+} = 10.0$ . The surface energy of the  $\alpha\beta$  interface is taken to be 1.0.

## 3.1 Boundary and initial Conditions

- Voltage of the boundary is Dirichlet in "y" direction and no-flux in "x" direction. The geometry of the pit is initialized as perturbed planar interface. The perturbation is of one wave length which is equal to the width of the system in the x-direction. The half wave length becomes the width of pit and amplitude in the y-direction becomes the depth of the pit. Voltage at the substrate boundary in the y-direction is kept at a constant voltage of 1.0 while at the electrolyte end it is kept at 0.

- The boundary conditions for the diffusion potentials are Dirichlet in the y-direction and no-flux in the x-direction.
- The boundary condition for the phase-field is no-flux in all directions.

## 3.2 Simulation studies

In order to follow the auto-catalytic nature of the mechanism of pitting reaction, let us follow the development of the  $Cl^-$  which is the principal component determining the rate of the dissolution reaction. In Fig.3.1, we see that with time the composition of  $Cl^-$  becomes increasingly non-homogeneous with the build-up occurring at the depressions of the pit geometry. From the model construction, this would increase the rate of the dissolution reaction in these areas. The reason of  $Cl^-$  build up is the build-up of  $Al^{3+}$  ions which are produced as a result of the dissolution reaction. Being a positive ion, this would naturally cause the build-up of positive charge that will attract the  $Cl^-$  ions from the bulk. This is a natural consequence of the solution to the electrostatic potential profile which ensures charge neutrality. Thus, it is expected, given the low diffusivity of the  $Al^{3+}$  ions in the electrolyte, that confined regions such as that of a pit depression would eventually be sites where accumulation of the  $Al^{3+}$  ions would occur due to geometric confinement which would in turn cause in more  $Cl^-$  ions to arrive and fasten the reaction, thus revealing the auto-catalytic nature of the process.

Given this prelude, it is natural to expect that one of the major criteria influencing the reaction kinetics is indeed the geometry of the pitting. In our initialization procedure of the pit, we have two variables to alter the pit geometry, one is the width of the pit and the other is the depth.

Among the first studies that was performed was to change the width of the perturbation for the same initial depth. In the figures, Fig.3.2, compares two simulation results with same starting amplitude of 14 while the width is 20 in Fig.3.2a and 28 in Fig.3.2b.

In Fig.3.2 notice the difference in the interfacial shapes with time. While in the narrower pit, the reaction occurs faster causing the both sideways as well as downwards motion of the pit. Owing to the fact that the reaction rate is proportional to interface area that is activated, the sideways motion of the pit is larger than the vertical motion

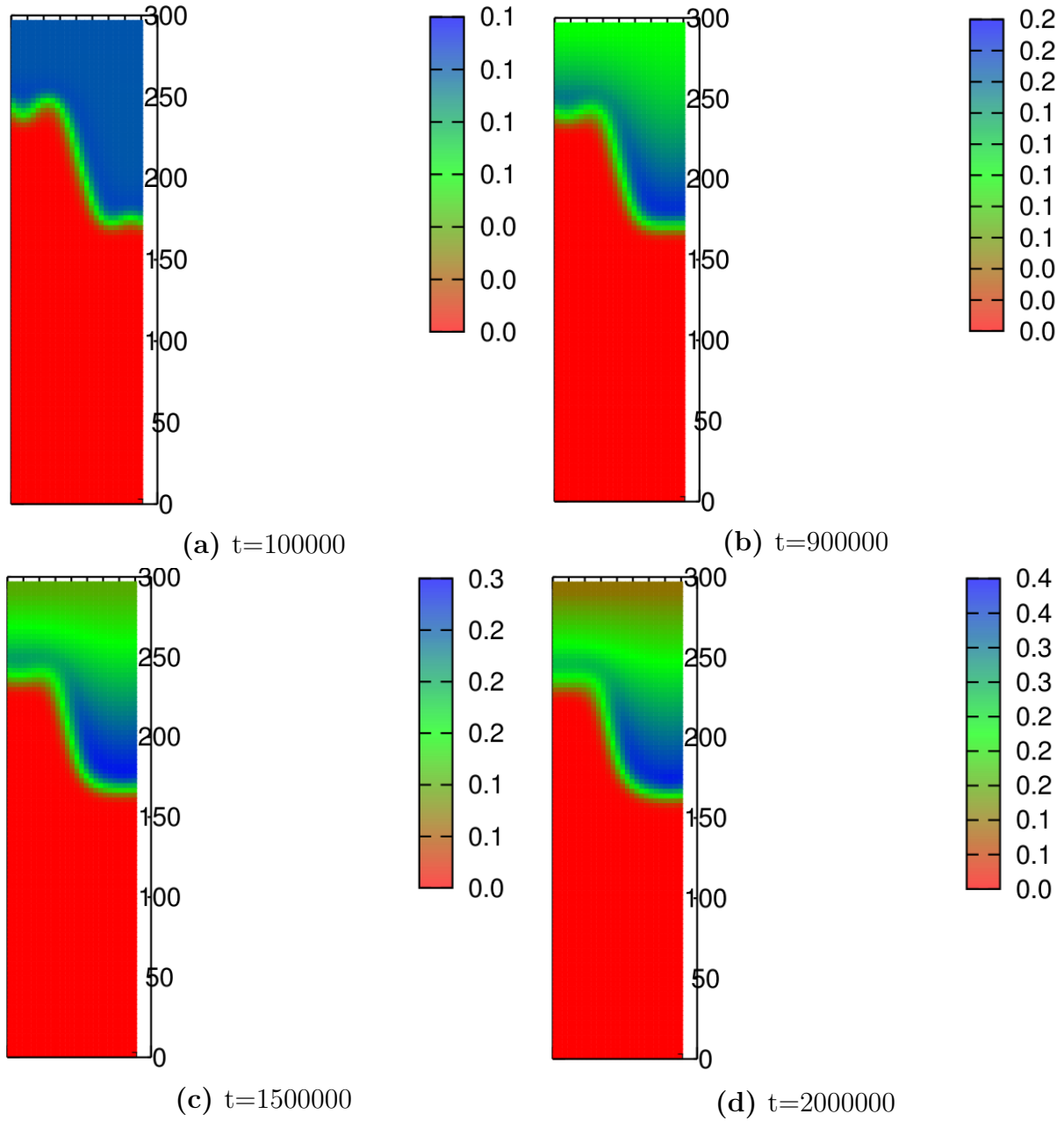


**Figure 3.1:** The red regions in (a) represent the substrate and the blue regions the electrolyte. From (a) to (d) the  $\text{Cl}^-$  concentration develops from an uniform composition in the electrolyte indicated by the blue color to a inhomogeneous distribution as the pitting reaction proceeds. This is evident with the higher concentration of  $\text{Cl}^-$  at the pit.

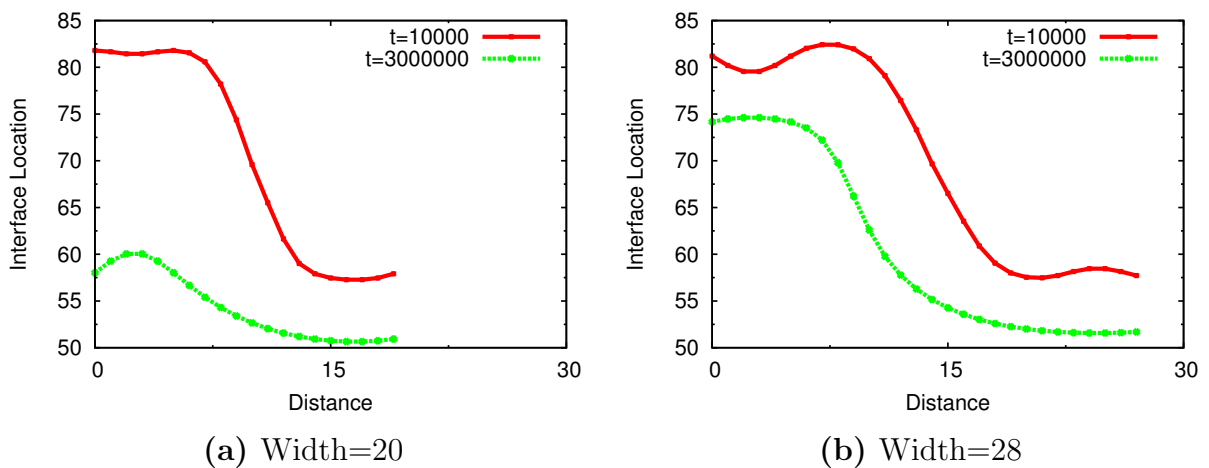


**Figure 3.2:** Plot showing the binary interface contour and its development over time. A comparison between initial and final condition for two different widths of the initial pit, in (a) width=20 and in (b) width = 28.

and thereby, the narrower pit also broadens faster. Given the limited geometry of the narrower pit, once the pit wall reaches the leftmost boundary, the reaction proceeds in a direction to flatten the pit.

In Fig.3.3 compares the evolution for two different depths at the same width and additionally comparing the difference in behavior between the pit-depths at two different widths.

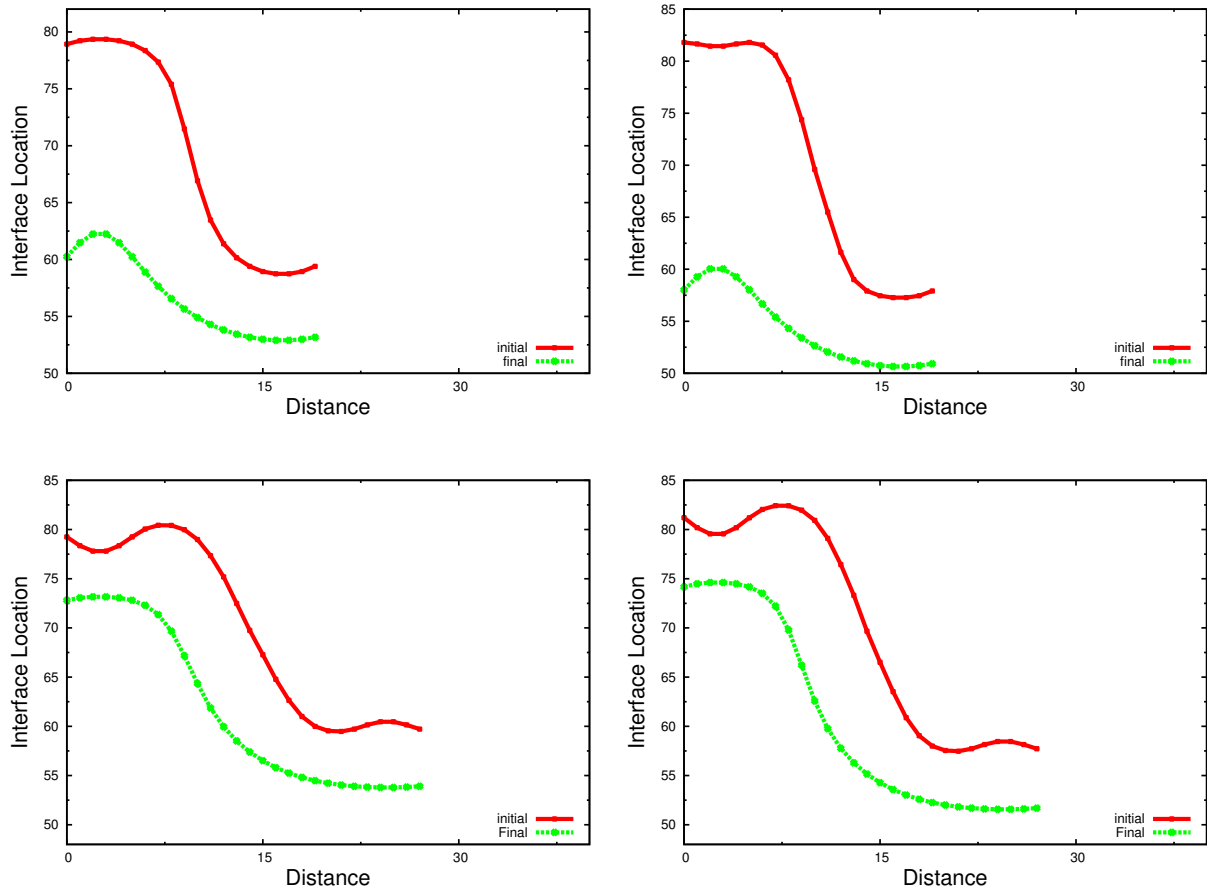


**Figure 3.3:** Plot showing the binary interface contour and its development over time. A comparison between initial and final condition for two different widths and depths of the initial pit, in (a) width=20, depth=12, (b) width=20, depth=14, (c) width=28, depth=12, (d) width=28, depth=14

As seen in the images the initial interface location is at the same position(vertically) but in the final position the bottom of the pit of width 20 have moved more in vertical direction, 6.2865 and 6.7055 respectively for depth 12 and 14, as compared to the pit bottoms of width 28, 5.4483 and 5.6579 respectively for depth 12 and 14. Due to the anodic reaction at the interface of substrate and electrolyte,  $Al^{3+}$  is produced, where due to confined geometry of the pit the concentration of  $Al^{3+}$  becomes higher than the electrolyte existing outside the pit. Since  $Al^{3+}$  is a positive ion it increases the electrostatic potential inside the pit and so reduces the electrochemical potential for  $Cl^{-}$  inside the pit, resulting into the migration of  $Cl^{-}$  into the pit, Hence increasing the

$Cl^-$  density in the pit in comparison to the electrolyte out of the pit. Concentration of  $Cl^-$  in the pit is comparatively lower in the wider pit than the concentration in narrower pit where due to the higher  $Cl^-$  concentration there is increased aggressiveness of the corroding media inside the pit, due to the model construction. Therefore, inside the pit, for the case of wider pit corroding media is lesser aggressive while in narrower geometry corroding media is more aggressive due to higher  $Cl^-$  concentration, due to the more aggressive environment in the pits corresponding to width 20 (Narrower geometry) have corroded more. Correspondingly, a larger depth also leads to larger confinement thereby, larger reaction rates which is observed for both widths. Also, the pitting reaction occurs both sideways and downwards, and the it can be seen from the corrosion of side walls, that in narrower pit geometry the sideways motion of the pit wall is more than that of wider pit geometry. We did a systematic study into the variation of the pit depths for different initial pit depths for a width of 28. Increasing the amplitude and the pit bottom is found to move 5.0052, 5.2387, 5.3435, 5.6580 for the pit depth 8, 10, 12, 14 respectively. In general, we can conclude that higher the parameter  $\eta = Width/Depth$ , lower is going to be susceptibility to corrosion and vice-versa.

### 3.3 Auto-catalytic nature

As in the preceding sections, it has been mentioned that “ $\eta = Width/Depth$ ” is one of the factors to control the rate of pitting reaction inside the pit. Throughout the pitting process the depth and width changes resulting into the change in “ $\eta$ ”, hence affecting the rate of reaction. If the “ $\eta$ ” decreases with time the rate of pitting process will increase and vice-versa. To capture this information the interface profile at different time steps have been plotted keeping the time interval constant between two consecutive interface profile.

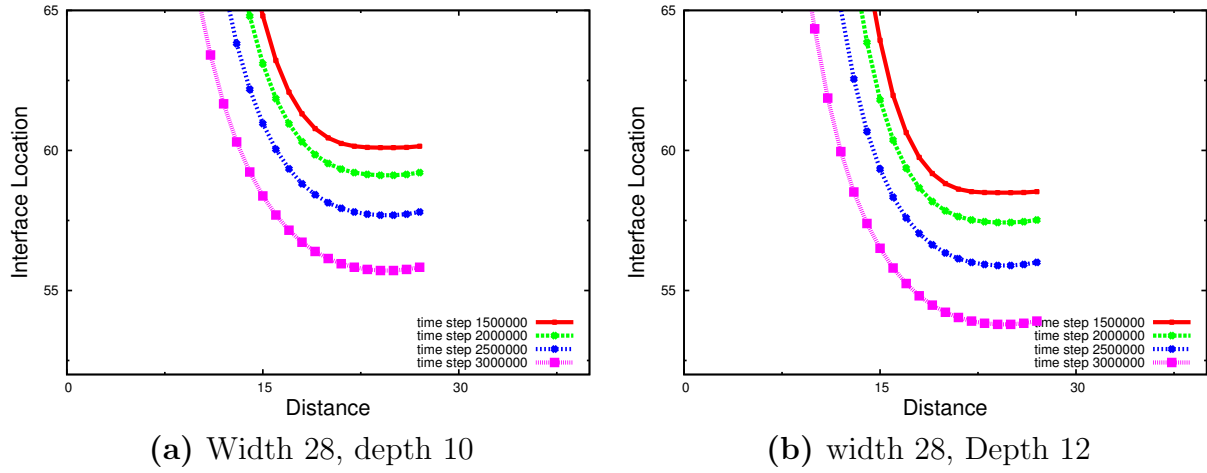


**Figure 3.4:** Interface profiles at various times, keeping the time interval constant between two consecutive interface profiles, in (a)width 28, depth 10 and (b) width 28, depth 12

Fig.3.4b and Fig.3.4a are clearly showing that the vertical movement of pit bottom is increasing as the depth is increasing. From the figures we can conclude the auto-catalytic nature of pitting reaction.

# Pitting in three-phase regions

In the context of susceptibility to corrosion, three-phase regions are natural sites for electrochemical attack as these offer for natural confined regions. Such regions occur quite frequently in materials science such as at grain-boundaries, matrix-precipitate interfaces etc. From Mullins' theory it is known that the when a two-phase boundary intersects the flat free surface it longer more remains in the equilibrium with the surfaces, owing to lack of balance of forces of the surface tensions. A natural angle (dihedral angle of  $\gamma_{gb} = 2\gamma_s \cos(\theta)$ ) develops between the surface tensions at the triple-junction for mechanical equilibrium that gives rise to a notch at the interface, which thereafter deepens on account of material transfer from the notch to the outer surface on either side of the two-phase boundary. This transport process is driven by curvature gradients and gives rise to the natural process of *grooving* in three-phase regions. These, grooves thus provide for natural sites for corrosion.

Continuing with the spirit of the preceding chapter where we see that the shape and geometry of the pit determines the pitting rates and in general susceptibility to pit deepening and broadening, for the case of three-phase region geometry, the physical parameter which determines the shape of the pit, are the relative values of the two-phase boundary energies, which we will refer to as  $\gamma_{gb}$  and the electrolyte substrate interface as  $\gamma_{sl}$ . Larger  $\gamma_{gb}$  energies gives rise to shallower pits and vice versa for larger  $\gamma_{sl}$ .

In order to perform the simulations using the multi-phase-field models we choose three order parameters  $\phi_\alpha, \phi_\beta, \phi_\gamma$ , where  $\alpha$  and  $\beta$  represent two substrates which are both similar in physical properties with respect to reaction with the electrolyte that is  $\gamma$ . The interfacial energies of the  $\alpha\beta$  interface is  $\gamma_{gb}$  while that of the  $\alpha\gamma$  and  $\beta\gamma$  interface is  $\gamma_{sl}$ . With this the evolution of the three-phase fields and the diffusion potentials can be derived using the evolution equations described in the section discussing the phase-field model.

## 4.1 Grooving

For the case of just illustrating the grooving process, we show the geometries at different times due to the grooving process in Fig.4.1, where we have varied  $\gamma_{sl}$  while holding  $\gamma_{gb} = 1.0$ . For shallower grooves (lower  $\gamma_{sl}$ ), the rate of grooving is faster.

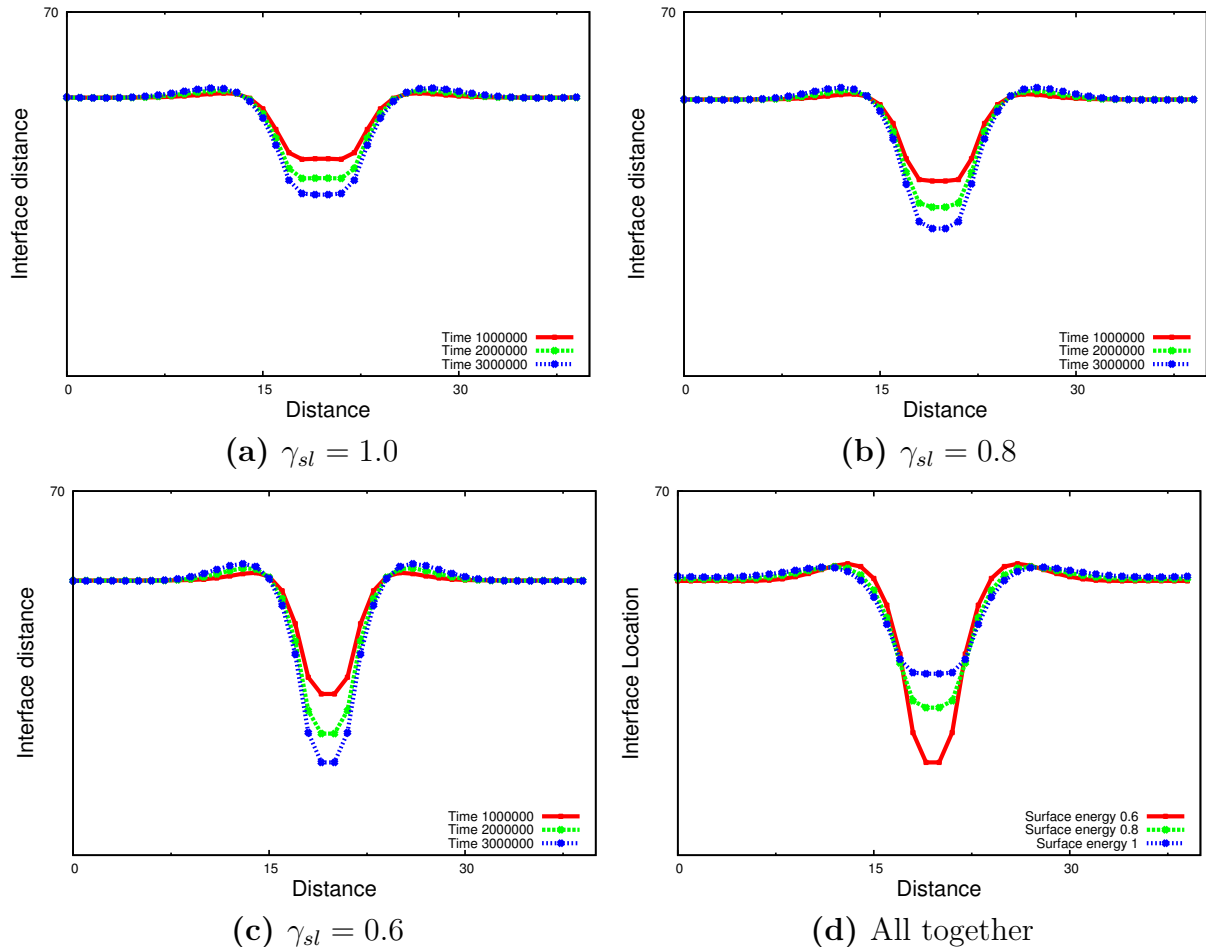


**Figure 4.1:** Plots showing the interface position at different times during the grooving process for different values of  $\gamma_{sl}$ , in (a)  $\gamma_{sl} = 1.0$ , (b)  $\gamma_{sl} = 0.8$ , (c)  $\gamma_{sl} = 0.6$  and (d) shows the compares all the interface positions at a given time.

## 4.2 Grooving coupled with pitting

Since, the thermal grooving produces pit like geometry it is interesting to test the geometrical effect of groove on the electrochemical attack, so the electrochemical attack is coupled with the grooving process. The first of the studies in this respect is performed for the case where we vary the shape of the triple-point region and compare the evolution of the groove-pit geometry with just the grooving dynamics.

Fig.4.2 outlines the phase-contours for the case of just grooving compared to that with the electrochemical attack. Contrary, to our intuition, not all pit geometries are prone to susceptible to increased corrosion, as seen in the Figs.4.2a and 4.2b. The



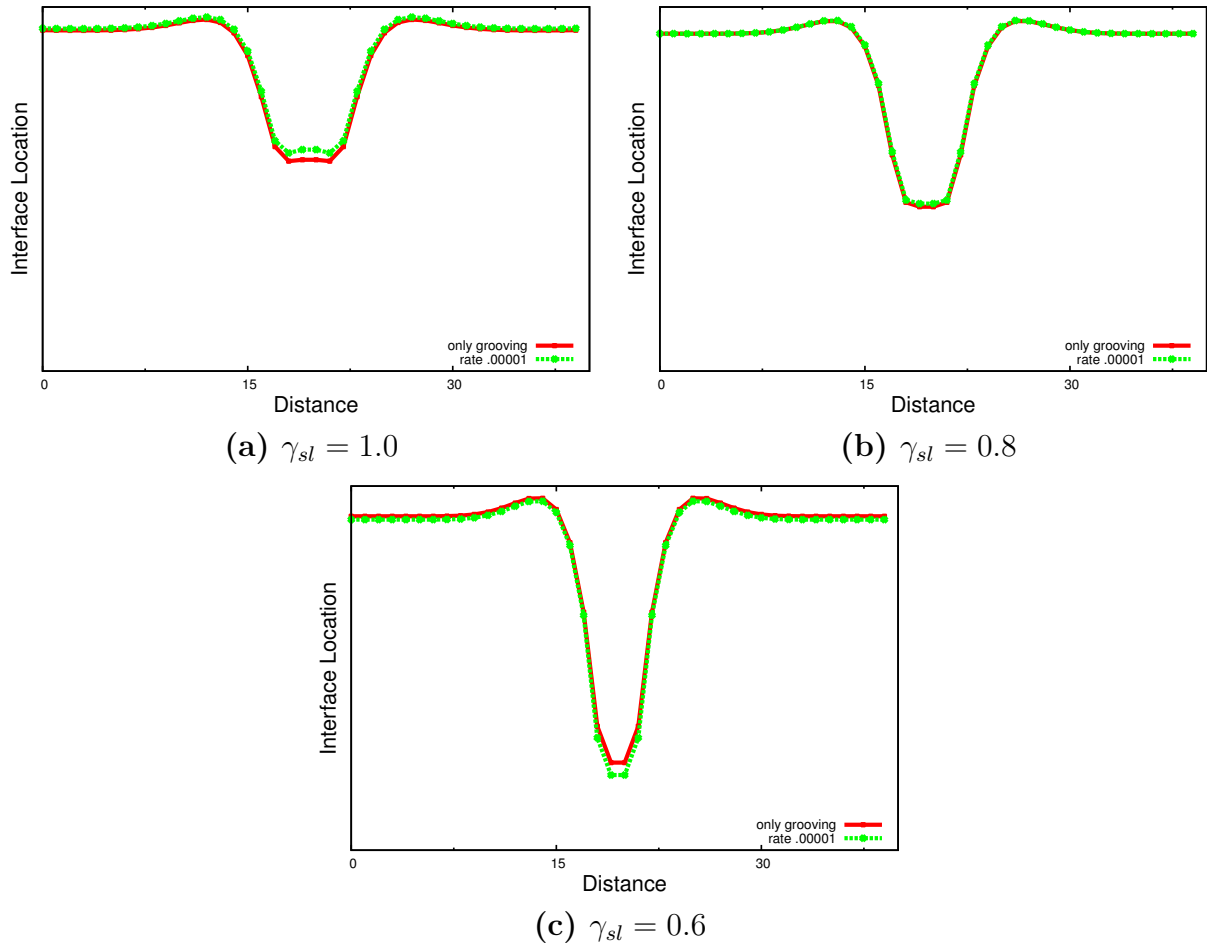


**Figure 4.2:** Plot showing the binary interface contour and comparison between the cases of electrochemical attack in combination with grooving, with just the grooving process, for three different triple point geometries created by the choice of three different values of the surface energies  $\gamma_{sl}$ , which is for (a)  $\gamma_{sl} = 1.0$ , (b)  $\gamma_{sl} = 0.8$  and (c)  $\gamma_{sl} = 0.6$ . The plots are normalized to bring out the differences between the evolution process brought about due to electrochemical corrosion.

reason for this, has got to do with the grooving process in general and the nature of the electrochemical reaction. Firstly, the grooving process is driven by curvature gradients, and therefore, any change in the shape of the interfaces, which is presently brought about the electrochemical reaction, will bring about a change in the grooving dynamics. This is seen by the flattening out of the groove hillocks due to the electrochemical reaction thereby reducing the driving force for mass transport by grooving. Therefore, there is actually an interplay between the dynamical effects of both the grooving and the electrochemical process. Secondly, as we move from the surface to the  $\alpha\beta$  boundary, the active surface which can take part in the reaction process becomes smaller and thereby the reaction rate also drops.

The geometry effect of the corrosion process does show up for the shallowest of pits as seen in Fig.4.2c, where the combined effects of grooving and pitting leads to the deepening of the pit in larger magnitude than just the grooving process.

Comparison of the coupled effects of grooving and pitting for different combinations of the rate constant controlling the dissolution reaction leads to varied evolution of the interfaces as highlighted in Fig.4.3. We see that although, there is enhanced attack at the surfaces due to increase in the rate constants, this does not necessarily bring about an increase in the pit deepening and broadening rates due to coupled interplay of the electrochemical attack and the grooving mechanism. Although, we have not tried out higher rate constants, it is quite possible that for a higher value we would see deepening of the pit depths that is the electrochemical attack aiding the grooving process.

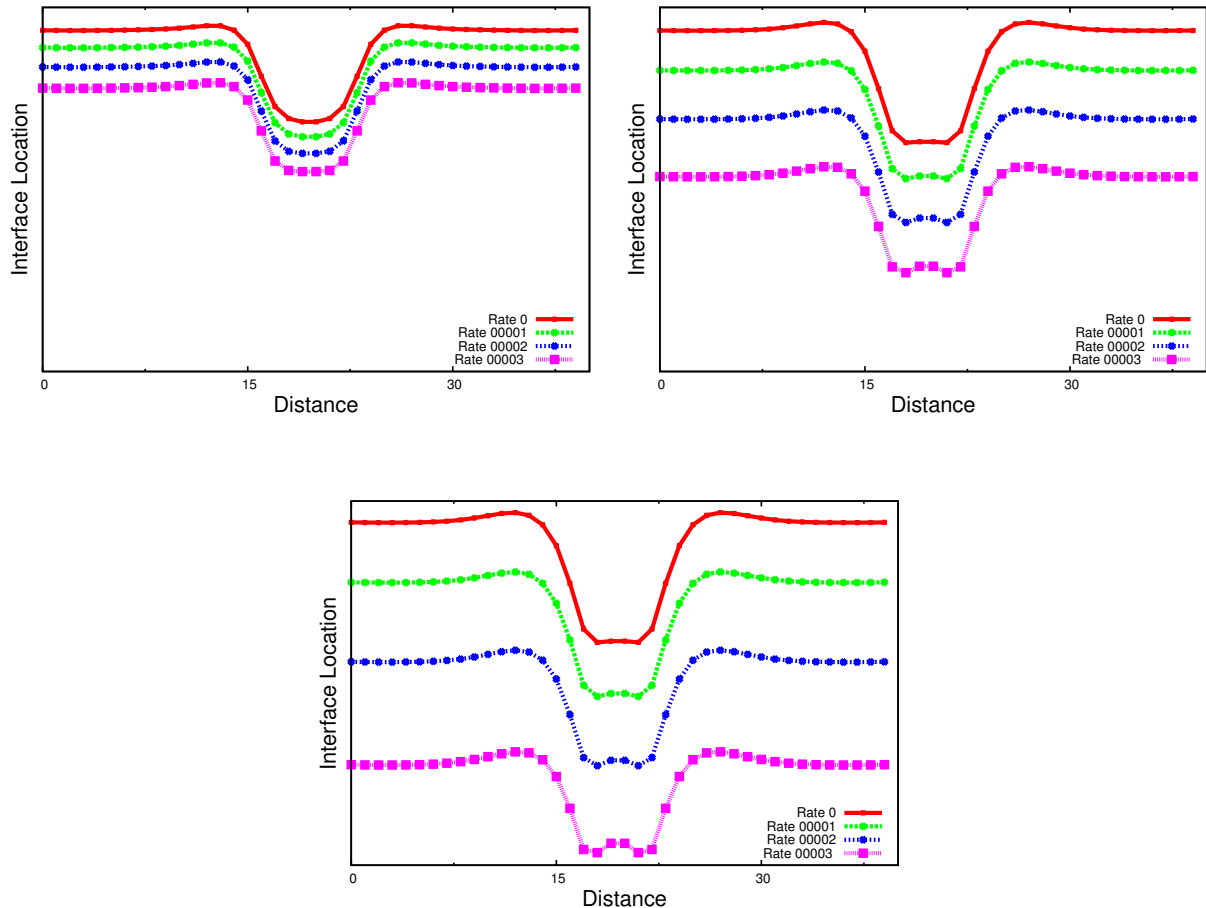


**Figure 4.3:** Plot showing the binary interface contour for different rate constants at separate times during evolution. In (a)  $t=500000$ , (b)  $t=1000000$ , (c)  $t=3000000$ .

In conclusion to this part of the analysis, the major result is that the pit shape that is a result of the interfacial energies controls not only the grooving process but also the electrochemical attack. Also, since the grooving process is connected to the interfacial shapes, there is inherent coupling between both phenomenon. Therefore, the effect of interfacial energies on the corrosive attack is non-trivial. But, we do conclude that shallower pit geometries arising from higher  $\gamma_{gb}$ 's are more susceptible to pitting at these locations.

### 4.3 Inter-Granular corrosion

In continuation, with the previous studies involving attack at the three-phase regions, we address a specific form of corrosion where there is concentrated attack at the grain-boundaries due to depletion of the protective element, occurring due to specific reactions at the grain-boundary. While this form of corrosion is not purely a result of the accumulation of charges in a confined geometry as we see in pure pitting, however, such local sensitization of the material through other coupled reactions may lead to

pitting type auto-catalytic nature of the reaction to occur at such boundaries. One such type of corrosion is Inter-granular corrosion. Inter-granular corrosion (IGC) is a form of localized corrosion in which grain boundary is less corrosion resistive than the other part of the surface of material. One such case is frequently seen in the case of stain less steel in which stain less steel is heated up to an elevated temperature and cooled slowly, that results into the diffusion of carbon towards grain boundary and it reacts with  $Cr$  at and near the grain boundary and forming the chromium carbide, rendering the grain boundary and nearby areas depleted of free  $Cr$  and making prone to electrochemical attack.

### 4.3.1 Model modifications

In order to model this phenomenon with the multi-phase model we again choose a three-order parameter model referring to the same structure of phases as in the preceding section. The only modification we bring about is to add an additional element which is  $Cr$  (please note this is just for a name and not signifying to any specific property of the element). The equilibrium concentration of this element in the substrate phases  $\alpha$  and  $\beta$  is 0.1 and in the  $\gamma$  phase is 0.0001. The thermodynamic coefficients of the free-energy densities in the two phases can therefore be derived as described in the phase-field section. In our construction this element which are calling  $Cr$  is meant to protect the substrate phases. To address the localized sensitization of the  $\alpha\beta$  boundary, we introduce an additional coupled reaction which depletes the  $Cr$  content. This reaction is assumed to be of the first order type and the reaction rate is written as,

$$R_{Cr} = j_{Cr} C_{Cr} \phi_{\alpha} \phi_{\beta}, \quad (4.1)$$

where  $j_{Cr}$  is a rate of the reaction, and the factor  $\phi_{\alpha} \phi_{\beta}$  limits the reaction rate to the  $\alpha\beta$  grain boundary. To capture the sensitization process, the reaction pertaining to the dissolution of the substrate occurs only below a particular level of  $Cr$  content.

### 4.3.2 Simulation studies

In the following we will characterize this localized phenomenon, on the basis of the influence of the anodic dissolution rates and the relative interfacial energies of  $\gamma_{sl}$  and

$\gamma_{gb}$ . Lastly, we will carry out the study, where the critical value for the sensitization is varied for different values of Cr content.

### IGC at various anodic dissolution rates

To simulate the grain boundary corrosion, two grains have been taken which are separated by a grain boundary. Below a critical value of Cr, the anodic dissolution rate is initiated. That gives a regions having very less amount of free  $Cr$  where the electrolyte can attack, in this phenomenon the region which has  $Cr$  more than a critical level is not attack by electrolyte or protected by  $Cr$ . This process is also coupled with grooving phenomenon, giving a geometric factor at the site of attack. The  $j_0$  (Butler-Volmer coefficient) for this reaction is again proportional to the departure of the  $Cl^-$  concentration from its equilibrium value. Thus, we also capture the confinement effects and therefore the auto-catalytic nature of pitting. Also, it is now additionally dependent on the inverse ratio of the  $Cr$  concentration from its equilibrium value, which will necessitate increased reaction rates where the  $Cr$  content is depleted.

Fig.4.4 depicts the process of inter-granular corrosion for different reaction rates. Notice, in contrast to the previous studies that were performed in the preceding sections, here no dissolution reaction occurs at the surface, while concentrated reaction occurs at the  $\alpha\beta$  boundary.

Comparing the individual profiles with the just the process of grooving, we see in Figs.4.5, that with increase rates of the anodic dissolution reaction, now there is increased attack at the three-phase regions. Concomitant with the increased depth of the pit, the width of the pits are also wider highlighting the influence of localized attack.

### IGC at various surface/ electrolyte interface energies

In the following sub-section, we elaborate on the influence of the change in geometry of the three-phase region on the corrosion rate. This has been performed as before by altering the relative values of the interfacial energies  $\gamma_{sl}$  and  $\gamma_{\alpha\beta}$ .

Fig.4.6 depicts the different evolution rates for the different conditions of differing surface energies. For lower surface/ electrolyte interface energy the groove geometry is sharper and narrower and the movement of pit root is more. The reason can be attributed to the fact to both the auto-catalytic nature of pitting discussed before in

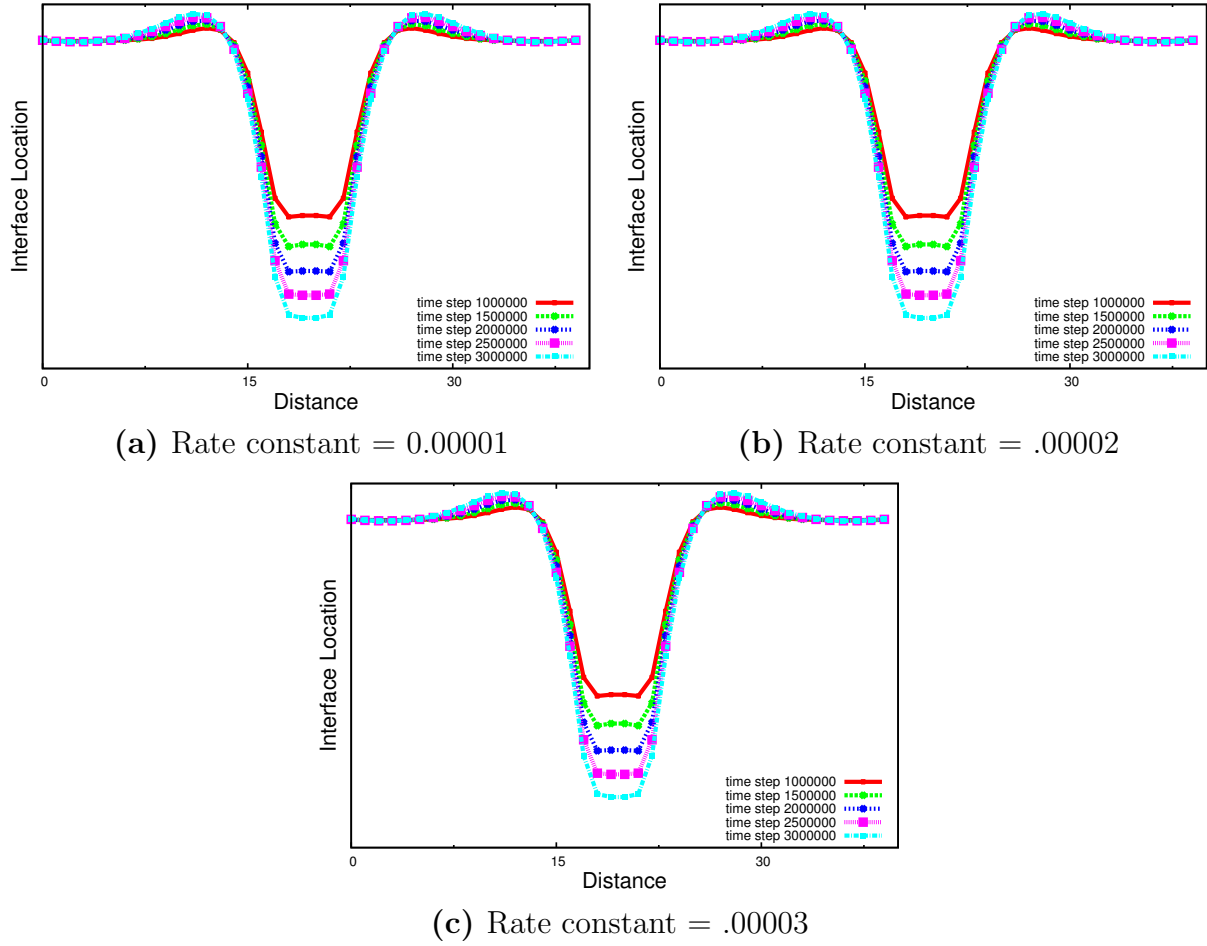


**Figure 4.4:** Interface contours plotting the progress of the inter-granular corrosion process for three different reaction rate constants for the dissolution process, in (a) rate constant = 0.00001, (b) rate constant = 0.00002 and (c) rate constant = 0.00003.

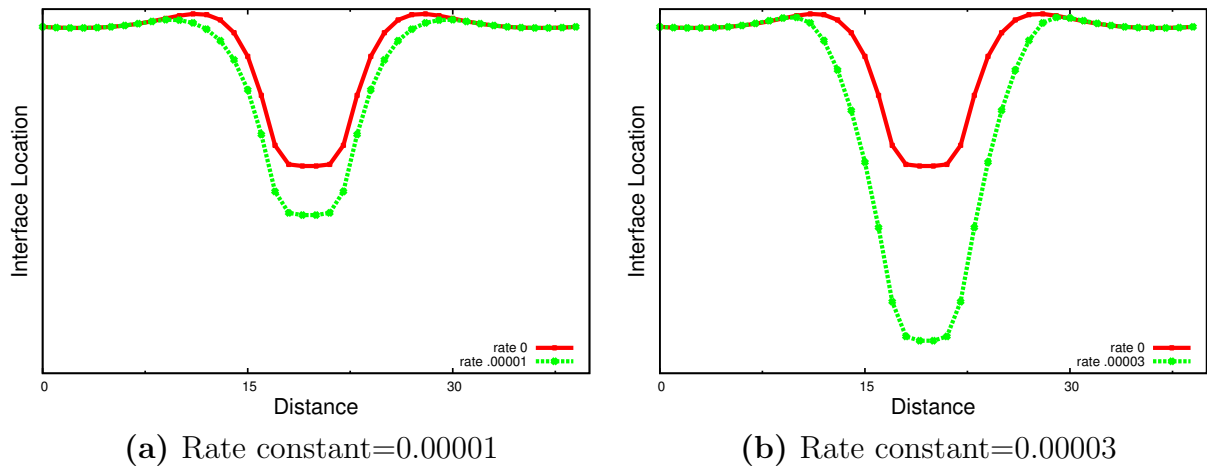


**Figure 4.5:** Interface plots showing comparison between the cases of pure grooving and under the influence of inter-granular attack for two different reaction rates, in (a) rate constant=0.00001, and (b) rate constant=0.00003.

the context of accumulation of  $Cl^-$  at confined geometries as well as the increased rate of the overall dissolution process because of the depletion of  $Cr$ .

### IGC at different $Cr$ content

Finally, we study the effect of  $Cr$  concentration, the critical  $Cr$  concentration beyond which the dissolution reaction is activated is varied. Since, the simulation has been

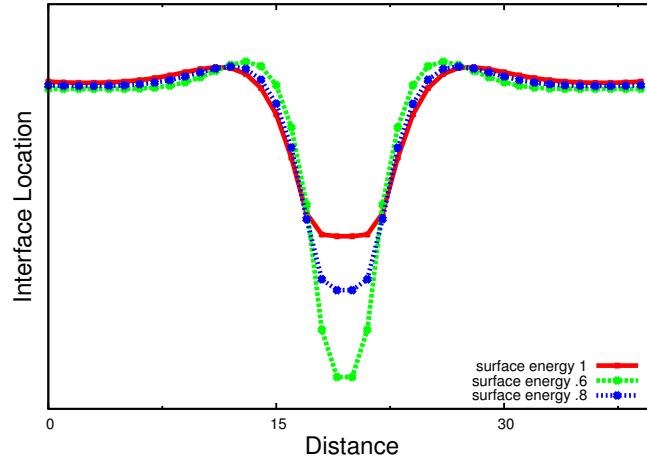


**Figure 4.6:** Comparison of IGC for rate constant= .00001 for various surface energy values

coupled with the grooving process, grooves are formed due to the surface energy driving force. The walls of grooves are attacked only if the concentration at the walls are so that it becomes lesser than the critical limit. In Fig.4.7 we see that with increase in time the depletion of the  $Cr$  occurs which leads to the localized attack to occur which is shown in 4.7c. For lesser times, as shown in Fig.4.7a and 4.7b the reaction rates the  $Cr$  concentrations are still higher than the critical value of  $Cr$  below which sensitization occurs.

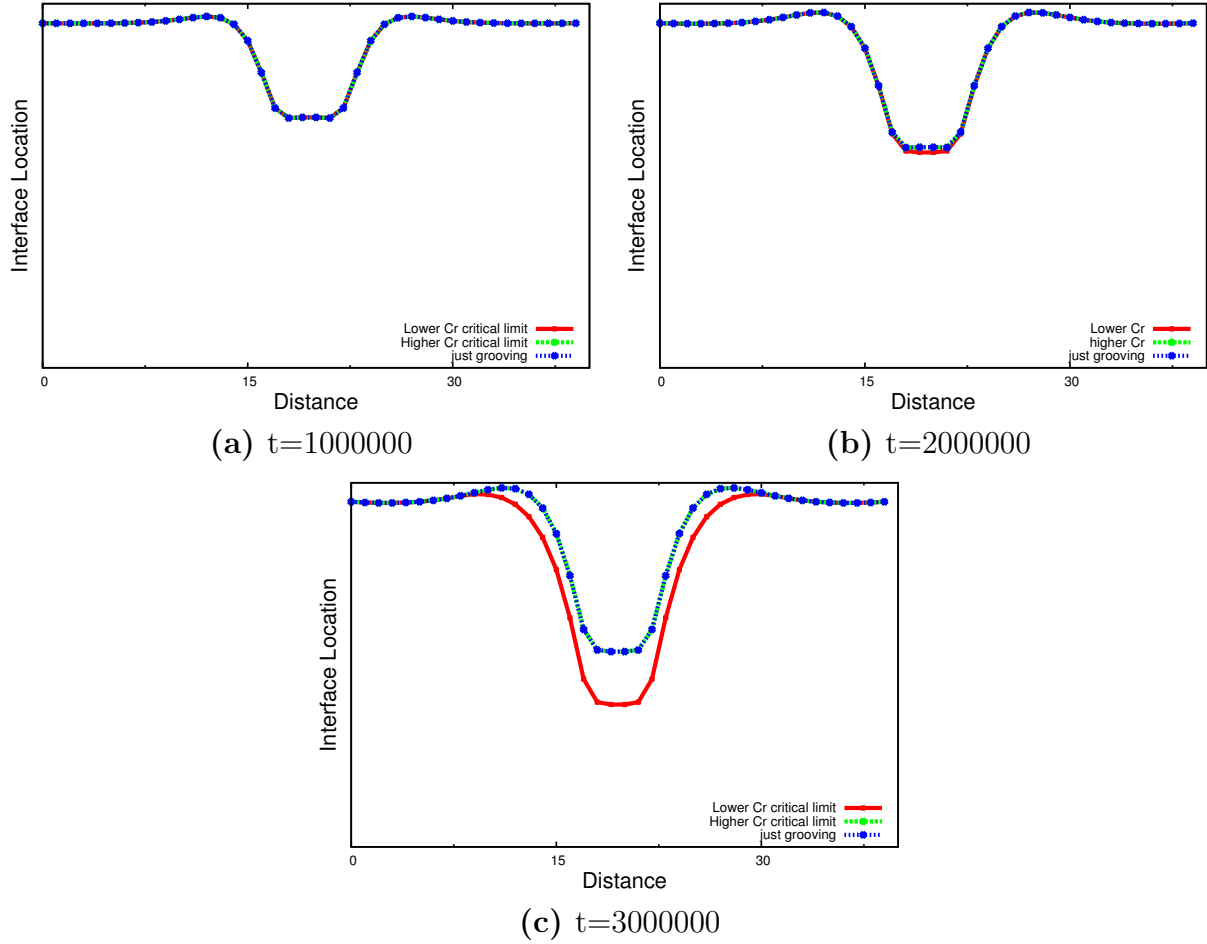


**Figure 4.7:** Interface profiles showing the pit formation at different times for three different conditions of just grooving and two different values of critical concentration of Cr below which the pitting reaction is activated. In (a) and (b) which are plots corresponding to time  $t=1000000$  and  $t=2000000$  respectively, there is no difference in the evolution between the plots showing jut grooving dynamics and electrochemical attack, while in (c) which is for  $t=3000000$ , there is increased pit formation for the case of lower Cr content.



# Conclusions

In this thesis work, we have been able to formulate a generic phase-field model for modeling pitting corrosion. In particular, we have been able to propose a model which captures the auto-catalytic nature of the pitting process. Using the model thereafter we have been able to highlight the characteristics of the pitting reaction in particular linked to the geometrical characteristics of the pit. Although, we do not include all the homogeneous reactions occurring in the electrolyte and which are implicitly linked to the modifying the pitting rate, our approach is generic enough to be able to account for these reactions as well.

Using the model we have probed the case of electrochemical attack at grain boundaries as well as attack on particular sensitized regions due to coupled reactions leading to depletion of protective elements. We have characterized such reactions again based on the geometrical nature of the three-phase regions, which are in turn related to relative values of the interfacial energies.

Further, through our work we point out that it is not always that the coupled effect of pitting and localized corrosive attack gives rise to detrimental pitting reactions, Here as well, both the shape of the groove as well as the aggressiveness of the electrochemical reaction determine the rate of the pitting reaction.

# Bibliography

- [1] L. Balazs and J. F. Gouyet. *Physica A*, 217:319–338, 1995.
- [2] L.Q. Chen. *Annual Review in Materials Research*, 32:113–40, 2002.
- [3] A. Choudhury and B. Nestler. *Phys.Rev.E*, 85:021602, 2011.
- [4] H. Garcke, B. Nestler, and B. Stinner. *SIAM J Appl Math*, 64:775, 2004.
- [5] J. E. Guyer, W. J. Boettinger, J. A. Warren, and G. B. McFadden. *Physical Review E*, 69:021603, 2004.
- [6] J. E. Guyer, W. J. Boettinger, J. A. Warren, and G. B. McFadden. *Physical Review E*, 69:021604, 2004.
- [7] B. Nestler and A. Choudhury. *Current Opinion in Solid State and Materials Science*, 15:93, 2011.
- [8] B. Nestler, H. Garcke, and B. Stinner. *Phys. Rev. E*, 71:041609, 2005.
- [9] M. S. Park, S. L. Gibbons, and R. Arróyave. *Acta Materialia*, 61:7142–7154, 2013.
- [10] Y. Shibuta, Y. Okajima, and T. Suzuki. *Scripta Materialia*, 55:1095, 2006.
- [11] Y. Shibuta, Y. Okajima, and T. Suzuki. *Science and Technology of Adv. Mat.*, 8:511, 2007.
- [12] I. Steinbach. *Modeling and simulation in Mat. Sci. and Engg*, 17:073001–31, 2009.
- [13] J. Xiao and S. Chaudhuri. *Electrochimica Acta*, 56:5630–5641, 2011.